Signatures of Topological Superconductivity in Bulk Insulating Topological Insulator $BiSbTe_{1.25}Se_{1.75}$ in Proximity with Superconducting $NbSe_2$: Supplementary Information

Abhishek Banerjee[1], Ananthesh Sundaresh[1], Rajamanickam Ganesan[1] and P. S. Anil Kumar[1]*

[1]*Department of Physics, Indian Institute of Science, Bengaluru 560012, India*

E-mail: anil@iisc.ac.in

A. Fabrication of devices

The fabrication of devices in this work starts with the preparation of heterostructure devices on Si/SiO_2 substrates. The Si substrates are p-type doped with a resistivity of $0.001 - 0.005$ Ω-cm coated with 285nm of dry chlorinated thermal oxide. The heterostructures are prepared using a using a dry Van der Waals transfer technique. First, thin flakes of $NbSe_2$ and topological insulator $BiSbTe_{1.25}Se_{1.75}$(BSTS) are exfoliated onto two separate pieces of 5mm×5mm silicon wafers using commercially available Scotch Tape (3M). A transparent polymer stack consisting of polypropylene-carbonate(PPC) spin-coated on polydimethylsiloxane(PDMS) films stuck to a glass substrate is fixed to a micromanipulator stage. Using a custom-built transfer setup, the polymer stack is used to 'pick up' a suitable $NbSe_2$ flake from the SiO_2 substrate. This flake is then aligned

*To whom correspondence should be addressed

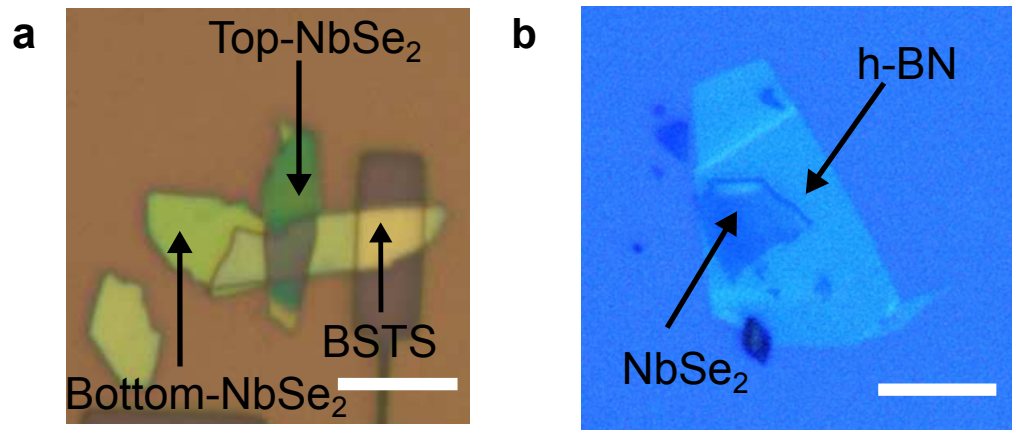

Figure S1: (a) Optical micrograph image of $NbSe_2$/BSTS junction device. Note that the top $NbSe_2$ layer is delaminated for our experiment, only the bottom $NbSe_2$/BSTS junction is probed in the main text. (b) Blue channel optical micrograph image showing an $NbSe_2$/h-BN bilayer device. Both devices are depicted prior to electrode deposition. Scale bar $= 10\mu$m

with micrometer precision to a suitable flake of BSTS. The glass substrate is lowered until the $NbSe_2$ and BSTS flakes are in contact. After desirable alignment and contact between the two flakes is established, the polymer stack is heated at $\sim 80^{\circ}$ C to melt the PPC layer which causes the $NbSe_2$ flake to 'drop down'. The residual PPC is later removed by cleaning the sample in chloroform and acetone. The entire exfoliation and transfer process is carried out within an Argon glove box with $<$0.1 ppm of Oxygen, ensuring that surface contamination effects due to oxidation and moisture are completely suppressed. Devices with other stacking configurations, such as h-BN/$NbSe_2$ are prepared using a similar protocol by suitably choosing the flakes of interest. The devices are then immediately coated with a bilayer poly-methyl-methacrylate (PMMA) resist consisting of PMMA-495 A4 (spun at 3000rpm for 30s) and PMMA-950 A2 (spun at 3000rpm for 30s). S1 depicts two of the devices reported in this work prior to contact deposition. This is followed by e-beam lithography to define contact lines. Prior to deposition of metal lines, the samples are milled in an Ar ion beam for 2 minutes to remove the native oxide that forms on the BSTS and $NbSe_2$ layers. Contact metal deposition of Cr/Au is then performed using e-beam evaporation.

B. Characterization of $NbSe_2$

$NbSe_2$ single crystals as large as 2-5mm are grown by chemical vapour transport with iodine as the transport reagent. $NbSe_2$ flakes are obtained by scotch-tape exfoliation within an argon filled glove box($<$0.1 ppm of O^2) and capped with insulating hexagonal Boron Nitride flake as shown in S2(a) and (b). Samples are subsequently fabricated into devices by e-beam lithography and deposition of Cr/Au(10nm/70nm) contact lines. S2(c) shows the resistance versus temperature measurement of a typical $NbSe_2$ device showing a sharp superconducting transition at $T_c = 7.1K$ and a resistance bump at $T_{cdw} \simeq 33K$ due to charge density wave ordering. The sharpness of the superconducting transition shown in S2(d) ($\delta T \simeq 0.3K$) and the presence of a clear charge-density wave transition attest to high quality of our $NbSe_2$ samples. Mangetoresistance measurements, shown in S2(e) show an upper critical field $H_{c2} \simeq 4T$ which coincides with values reported in literature.

The residual resistivity ratio obtained as R(300)/R(7K) $\simeq$ 16 shows that our samples are in the low disorder regime. This is characteristic of the single crystalline nature of $NbSe_2$ compared with bulk superconductors like Nb, W and Al that have been previously used to study proximity effects on topological insulators. Additionally, the layered nature of this material lends it an intrinsically two-dimensional Fermi surface. This is also unlike bulk superconductors where the Fermi surface is always three-dimensional. The two-dimensionality of the Fermi surface of $NbSe_2$ matches well with the intrinsically two-dimensional topological surface states, and provides an avenue towards large wave-function overlap and strong proximity effects.

C. Blonder-Tinkham-Klapwijk fitting

The current I_{ns} through a normal metal/superconductor(N/S) interface carries two components. The first component refers to the process of *normal reflection* of electrons at the normal metal/superconductor interface due to a lack of electronic states within the superconducting gap. The second component, known as Andreev reflection describes the possibility that an electron impinging on the N/S interface can get converted to a Cooper pair and gets retro-reflected back as a hole. This process is not really a *reflection*, in that it can be though of as two coherent electrons on the normal metal

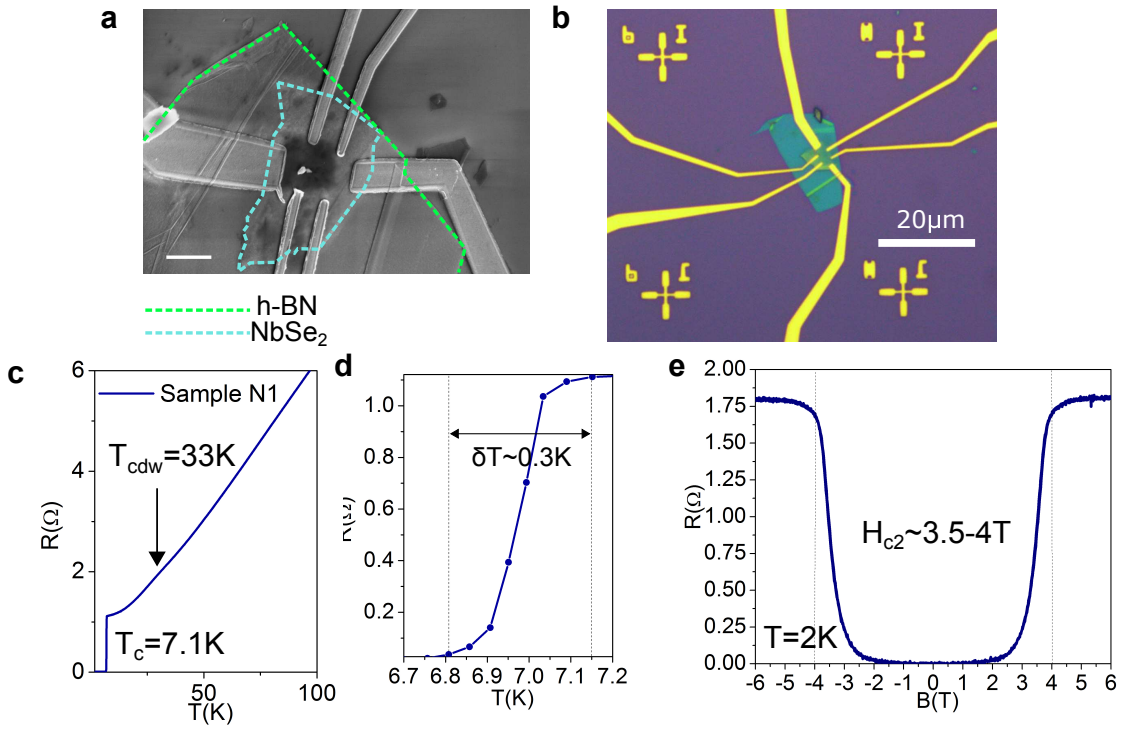

Figure S2: (a) Scanning electron microscope image of device fabricated on $NbSe_2$ flake capped with hexagonal Boron Nitride. Scale bar = 2 μm (b) Optical micrograph image of the same device. Scale bar = 20 μm (c) Resistance vs temperature of $NbSe_2$ flake showing the charge density wave and superconducting transitions (d) Width of the superconducting transition showing $\delta T \simeq 0.3K$ (e) Magnetoresitance at $T = 2K$ showing upper critical field $H_{c2} \simeq 4T$.

side combining to produce a Cooper pair on the superconducting side, and leads to enhanced conductance. Depending upon the potential barrier that exists between the normal metal and the superconductor, the current through the interface can either be blocked due to normal reflection or enhanced due to Andreev reflection. This leads to the Blonder-Tinkham-Klapwijk(BTK)[1] formula where:

$$I_{ns}(V) = C \int_{-\infty}^{\infty} [f(E) - f(E - eV)] [1 + A(E) - B(E)] dE \tag{1}$$

where V is the applied bias across the interface, E represents quasiparticle energy, $f(E)$ is the Fermi function, $A(E)$ is the probability for Andreev reflection and $B(E)$ is the probability for normal reflection. The constant C depends on various factors including the contact area and density of states of the normal metal which is assumed energy independent. The factors $A(E)$ and $B(E)$ are expressed in terms of coherence factors u_0 and v_0, where inelastic effects due to finite temperature

are incorporated by adding an imaginary decoherence term to the energy :

$$
\begin{aligned}
u_0^2 &= \frac{1}{2}\left[1+\frac{\sqrt{E+i\gamma)^2-\Delta^2}}{E+i\Gamma}\right] \\
v_0^2 &= \frac{1}{2}\left[1-\frac{\sqrt{E+i\gamma)^2-\Delta^2}}{E+i\Gamma}\right] \\
\gamma &= u_0^2+(u_0^2-v_0^2)Z^2 \\
a &= u_0 v_0/\gamma \\
b &= -(u_0^2-v_0^2)(Z^2+iZ)/\gamma \\
A &= |a|^2 \\
B &= |b|^2
\end{aligned}
\tag{2}
$$

The results of fitting our experimental differential conductance data normalized with the data at $T = 10K$ is shown in S3. Best fits are obtained with a lead resistance of $R_l \simeq 4000\Omega$. The extracted superconducting gap $\Delta \simeq 1.2meV$ which matches exactly with the superconducting gap of $NbSe_2$, $\Delta_{NbSe_2} \simeq 1.1-1.2$meV. With increasing temperature, the superconducting gap decreases while the thermal smearing parameter Γ increases as shown in S3(k) and S3(l) respectively.

At this point, we note that the interface transparency factor $Z = 3$ derived from our fitting implies that our BSTS/$NbSe_2$ interface is not highly transparent.This implies that our superconductor-TI junctions are not quite transparent.Yet, previous experiments, where other materials such as Nb have been used as the superconducting lead,[2,3] fail to produce any of the interesting features that we have observed in our experiments. It is possible that the perfect two-dimensional interface between the two materials at the van der Waals junction, resulting in strongly coherent exchange of Cooper pairs between the superconductor and the topological surface state, leads to a strong superconducting proximity effect in our experiments. The role of clean epitaxial interfaces to obtain strong proximity effects has been recently demonstrated in epitaxial Al-InAs nanowire junctions.[4] Niobium, because of its inherent three-dimensional and granular nature, and its strong proclivity towards bulk oxidation, is perhaps unable to form such clean two-dimensional interfaces with

topological insulators.

There is an additional interesting point, that one must consider when trying to generate topological superconductivity by proximity effect. To induce strongest topological superconductivity, it has been shown that there must be a balance between the strength of the superconducting proximity effect and segregation of the semiconductor and the superconductor so that the inherent properties of the semiconductor (such as strong spin-orbit coupling) are also retained. This criteria is satisfied when the electron spends equal times in the semiconductor and the superconductor, and is achieved by choosing an optimal value of barrier thickness separating the superconductor from the semiconductor. In recent experiments on topological superconductivity induced on Al/InAs 2D quantum wells,[5] the Aluminum layer was separated from the 2DEG layer of InAs by an insulating barrier of InGaAs. In these experiments, it was found that there is an optimal value of the thickness of the insulating barrier that leads to maximum topological superconductivity. This criteria should be applicable also to topological-insulator/superconductor junctions. Perhaps our devices are in such a regime where these criteria are satisfied. Additional experiments, varying the transparency between BSTS and NbSe2 will be required to confirm these effects, and is beyond the scope of the present work.

D. Applicability of Blonder-Tinkham-Klapwijk fitting

Although we have used the BTK formalism to obtain reasonable fits to our experimental conductance data, we note that such a procedure cannot be fully justified. The fundamental objection to such a fitting procedure is that the BTK formalism assumes that the N side of the N/S junction is a three-dimensional metal. In our experiments, the metal is replaced with a topological insulator. While bulk conducting TIs can indeed be approximated as good metals, the highly bulk insulating nature of our samples precludes such a description. In fact, the topological surface states are not only truly two-dimensional, but also they are *semi*-metallic featuring a linear dispersion around the Dirac point.

More importantly, Andreev reflection at the TI/SC interface presents a fundamental problem.

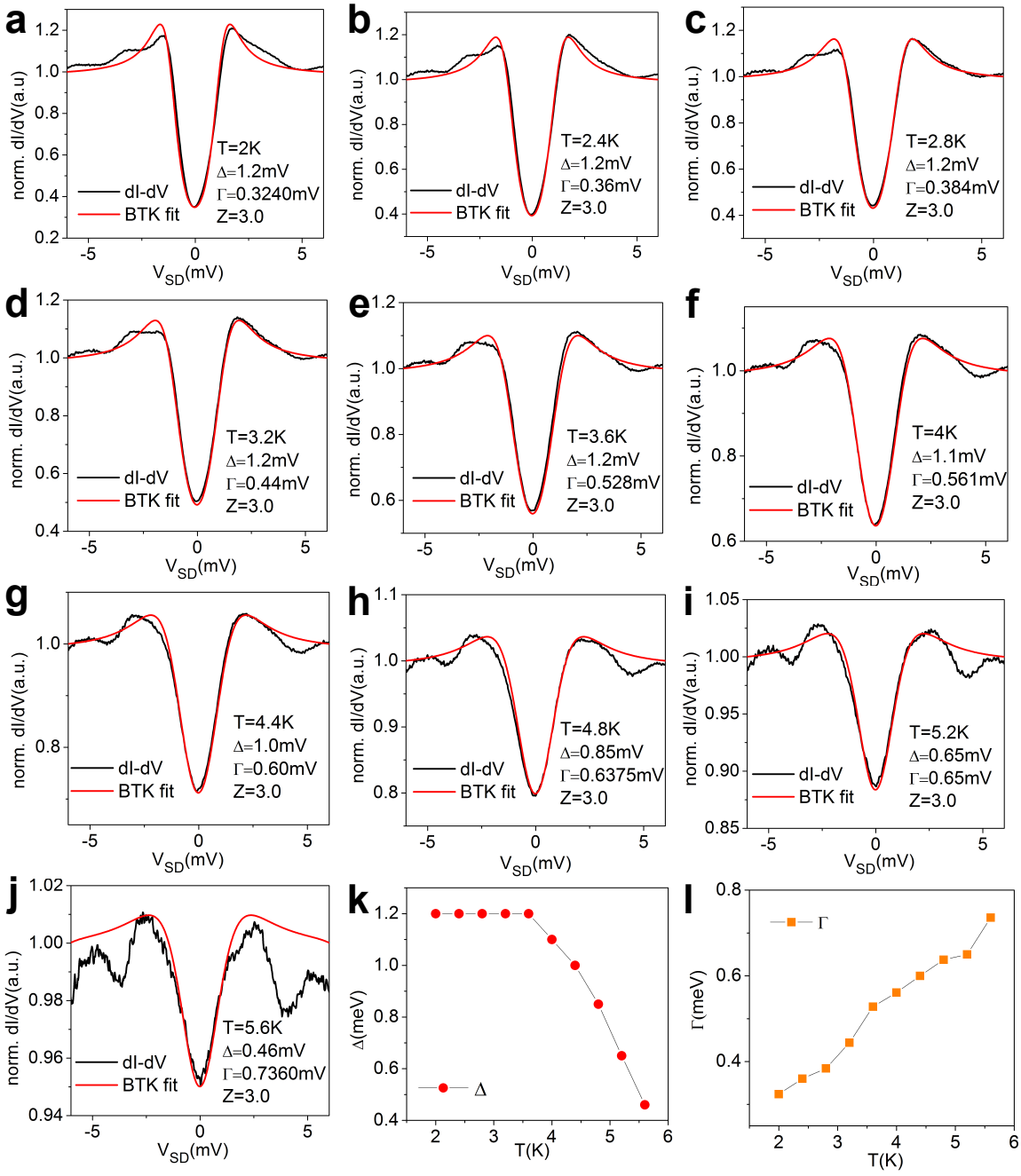

Figure S3: (a)-(j) BTK fitting of differential conductance data obtained at different temperatures from 2K-6K. (k) Δ and (l) Γ as a function of temperature

For an Andreev process to convert an electron into a singlet Cooper pair, it requires another electron moving with same momentum but with opposite spin. The spin-polarized surface state of a TI obviously forbids such a possibility. The only way such a process can therefore occur is if the

proximitized part of the TI/SC interface allows spin-triplet pairing, or if one considers that the electron with opposite spin-polarization is obtained from the *bottom* surface state where the chirality of spin-momentum locking is reversed. Several theoretical works have tried to study these issues, but the problem remains far from solved.

Finally, we note that although we obtain reasonably good fitting to the experimental data for low bias values(S3(a)-(j)), at higher biases, the fit cannot capture the experimental data at all. In fact, the intrinsic conductance asymmetry prevents a simultaneous fit to the both the coherence peaks. The conductance ripples at large biases are obviously not captured.

E. Theoretical modeling

To model the proximity effect between a conventional s-wave superconductor and a topological insulator, we evaluate the Bogoliubov-de Gennes Hamiltnonian and diagonalize it numerically to obtain the quasiparticle spectrum. We chose the four orbital ($|p_{Bi},\uparrow>,|p_{Bi},\downarrow>,|p_{Se},\uparrow>,|p_{Se},\downarrow>$) basis for representing the low-energy states of Bi_2Se_3. The corresponding *particle* Hamiltonian $h_0(k)$ is taken from Zhang *et al.*[6] The superconducting pair potential $\Delta(k)$ mixes the particle and hole states (represented by $-h_0^*(-k)$), giving the BdG Hamiltonian as follows:

$$H_{SC}(k) = \begin{pmatrix} h_0(k) & \Delta(k) \\ \Delta^\dagger(k) & -h_0^*(-k) \end{pmatrix} \tag{3}$$

where the normal state Hamiltonian h_0 for the topological insulator is given as:

$$h_0(k) = \begin{pmatrix} \varepsilon(k)+M(k) & 0 & A_1(k) & A_2^-(k) \\ 0 & \varepsilon(k)+M(k) & A_2^+(k) & -A_1(k) \\ -A_1(k) & A_2^-(k) & \varepsilon(k)-M(k) & 0 \\ A_2^+(k) & -A_1(k) & 0 & \varepsilon(k)-M(k) \end{pmatrix} \tag{4}$$

with

$$\varepsilon(k) = D_1(2-2\cos(k_z c)) + \frac{4}{3}D_2\left(3-2\cos\left(\frac{\sqrt{3}}{2}k_x a\right)\cos\left(\frac{1}{2}k_y a\right)\cos\left(k_y a\right)\right) - \mu$$

$$A_1(k) = A_1\sin(k_z c)$$

$$A_2^{\pm}(k) = \frac{2}{3}A_2 \times \left[\sqrt{3}\sin\left(\frac{\sqrt{3}}{2}k_x a\right)\cos\left(\frac{1}{2}k_y a\right) \pm i\left(\cos\left(\frac{\sqrt{3}}{2}k_x a\right)\sin\left(\frac{1}{2}k_y a\right) + \sin(k_y a)\right)\right]$$

$$M(k) = M_0 - B_1\left(2-2\cos\left(k_z c\right)\right) - \frac{4}{3}B_2\left(3-2\cos\left(\frac{\sqrt{3}}{2}k_x a\right)\cos\left(\frac{1}{2}k_y a\right) - \cos(k_y a)\right) \tag{5}$$

In the four-orbital basis, the superconducting pair-potential is a 4×4 matrix that can allow mixing between particle and hole states corresponding to any of the 16 pairs of basis states. This includes inter-orbital pairing between Bi and Se orbitals, or triplet pairings between channels with same spin. Fermi-Dirac statistics puts constraints on the allowed pair potential symmetries by requiring $\Delta^{lm}_{\sigma\sigma'} = -\Delta^{ml}_{\sigma'\sigma}$ to maintain wave-function antisymmetry.[7–10] This lead to four distinct pairing symmetries as shown in Table. S1. The actual pairing symmetry realized in the material will depend upon system dependent microscopic interactions.

Table S1: Superconducting pair potentials with different symmetries

Gap type	Pair potential values	Parity
Δ_1	$\Delta^{11}_{\uparrow\downarrow} = -\Delta^{11}_{\downarrow\uparrow} = \Delta^{22}_{\uparrow\downarrow} = -\Delta^{22}_{\downarrow\uparrow}$	Even
Δ_2	$\Delta^{12}_{\uparrow\downarrow} = -\Delta^{12}_{\downarrow\uparrow} = \Delta^{21}_{\uparrow\downarrow} = -\Delta^{21}_{\downarrow\uparrow}$	Odd
Δ_3	$\Delta^{12}_{\uparrow\downarrow} = \Delta^{12}_{\downarrow\uparrow} = -\Delta^{21}_{\uparrow\downarrow} = -\Delta^{21}_{\downarrow\uparrow}$	Odd
Δ_4	$\Delta^{12}_{\uparrow\uparrow} = \Delta^{12}_{\downarrow\downarrow} = -\Delta^{21}_{\uparrow\uparrow} = -\Delta^{21}_{\downarrow\downarrow}$	Odd

In S4, we present tight-binding results for the quasiparticle spectrum of a thin TI slab with the four different superconducting pair potentials described before. S4(a) shows the starting band-structure of the TI slab showing the gapless topological surface states along with five closely spaced bulk bands. S4(b) shows the quasiparticle excitation spectrum with chemical potential $\mu = 1$, but no superconductivity. Now we turn on superconductivity in our system and observe that the different pairing potentials produce different gap profiles. As shown in S4(c) and S4(e), the pair

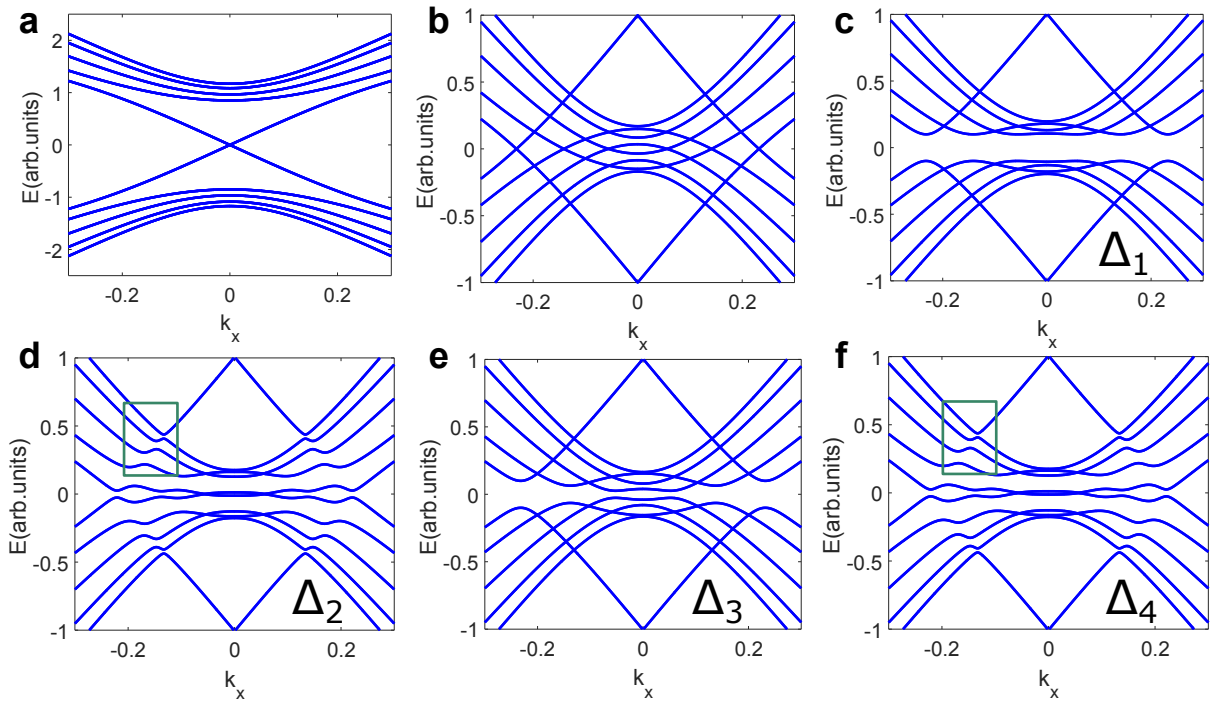

Figure S4: (a) Band-structure for a thin TI slab with 5 layers (b) Particle-hole excitation spectrum with $\Delta = 0$. Excitation spectra for proximitised TI slab with superconducting pair potentials given by (c) Δ_1 (d) Δ_2 (e) Δ_3 and (f) Δ_4. Green solid box indicates finite energy level anti-crossings between the topological surface state band and bulk derived bands. Parameters used for simulation: $A_1 = 1, A_2 = 1.5, B_1 = -0.5, B_2 = -0.75, D_1 = D_2 = 0, M = -0.8, \mu = 1, \Delta = 0.1$

potentials Δ_1 and Δ_3 open up a topological surface state gap with no mid-gap states. Also, no finite energy gaps due to avoided level crossings are observed.

On the other hand, S4(d) and S4(f) depict the formation of states within the superconducting gap at $E = 0$. These states are the surface Andreev bound states that exhibit a linear spectrum as expected for two-dimensional Majorana fermions. Symmetry constraints require the in-gap Majorana modes to continuously connect with the topological surface states at finite energy leading to a twisted quasiparticle dispersion known as the*butterfly* spectrum. While this feature has described in theoretical works before,[8,10] what has apparently eluded notice is the simultaneous presence of avoided level crossing as finite energies. These are marked as the 'green' solid boxes in S4(d) and S4(f). The avoided crossings appear *only when* the spectrum shows Majorana zero modes, and thereby provides a robust signature to ascertain the presence of topological superconductivity. In experiments where zero bias signatures of topological superconductivity are difficult to separate

from more trivial effects, the observation of finite energy gaps in density of states measurements can provide robust signatures of unconventional superconducting orders.

To aid comparison with experiment, we must evaluate the local density of states(LDOS) at the TI-SC interface which directly determines the differential conductance spectra. To evaluate the surface LDOS, we calculate the Green's function for the top surface of the superconducting TI slab.[11,12] This is performed by first considering an infinite crystal slab in the z direction, and then assuming a finite potential barrier for $z \geq z_0$. The lattice point z_1, just next to $z_0 > z_1$ represents the surface of the slab. The surface Green's function is then obtained from the bulk Green's function as follows:

$$G_b(z, k_{||}, \omega) = \frac{1}{N_z} \sum_{k_z} G_b(k_{||}, k_z, \omega) e^{ik_z z} \tag{6}$$

where the bulk Green's function is given as:

$$G_b(k_{||}, k_z, \omega) = (\omega + i\eta - H(k))^{-1} \tag{7}$$

The surface Green's function can now be obtained as:

$$G_s(k_{||}, \omega) = G_b(0; k_{||}, \omega) - G_b(a; k_{||}, \omega) \left\{ G_b(0; k_{||}, \omega) \right\}^{-1} G_b(-a; k_{||}, \omega) \tag{8}$$

The full spectral function and local density of states are therefore given as:

$$\begin{aligned} A(k_{||}, \omega) &= -\frac{1}{\pi} \sum_{\sigma=1-8} Im \left\{ G_s(k_{||}, \omega) \right\}_{\sigma\sigma} \\ \rho(\omega) &= \frac{1}{N_x^2} \sum_{k_{||}} A(k_{||}, \omega) \end{aligned} \tag{9}$$

In S5 we depict the full spectral function and the density of states evaluated for pair potentials Δ_1 and Δ_2 respectively. The spectral function for Δ_1 potential(S5(a)Left panel) shows a full gap at zero energy, while the topological surface state crosses the bulk derived bands without any mixing. The corresponding density of states(S5(a) Right panel) shows a full superconducting gap at zero

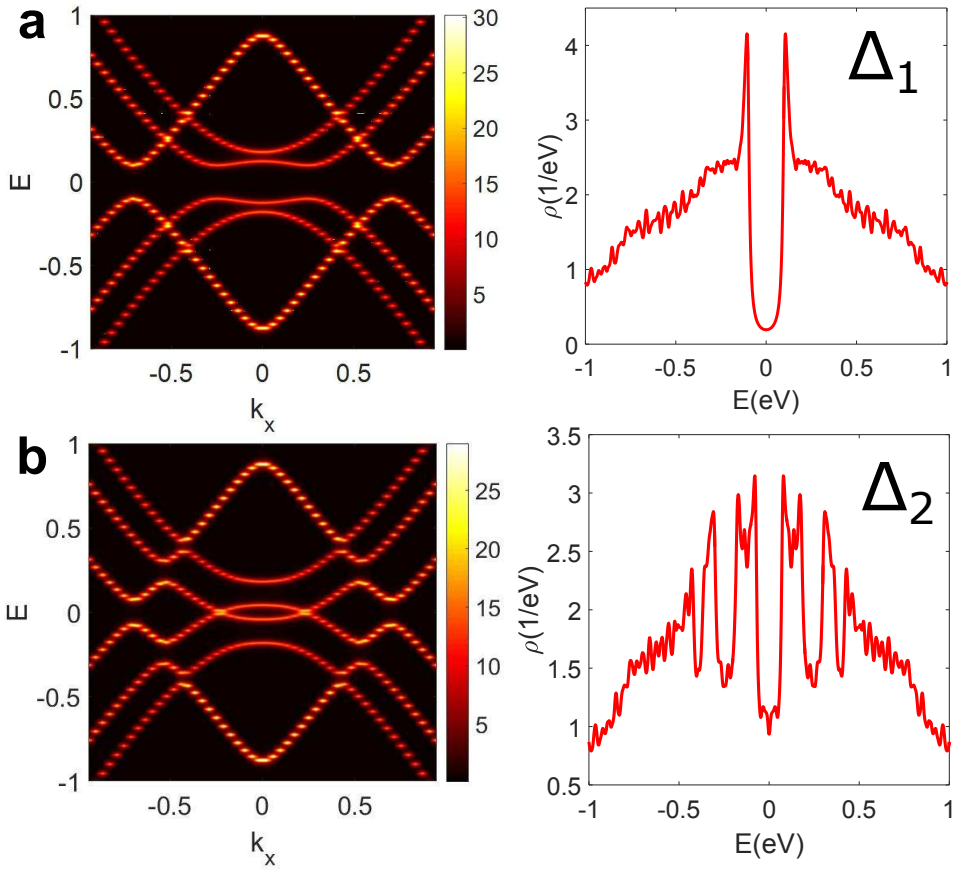

Figure S5: Spectral function(Left panel) and surface density of states(right panel) for a TI slab with superconducting pair potentials (a) Δ_1 and (b) Δ_2

energy and no features are visible above the coherence peaks at $E \simeq \pm\Delta = \pm$ 0.1eV. On the other hand, Δ_2 potential leads to an ungapped topological state at zero energy and prominent level anti-crossing at finite energy as shown in S5(b) Left panel. The corresponding density of states fully captures this effect as shown in the right panel of S5(b). Apart from a superconducting gap-like feature at zero energy, there are several mini-gaps at biases that are significantly larger than the superconducting pair potential($E \simeq \pm\Delta = \pm 0.1$eV). These gaps correspond exactly to the gaps opened up by level anti-crossing between the topological surface states and the bulk derived bands. Similarly, as shown in S6, potential Δ_3 produces a fully gapped state with no Majorana modes and the finite energy gaps are also absent. On the other hand, Δ_4 produces a Majorana mode at zero energy and also the associated finite energy gaps in the local density of states.

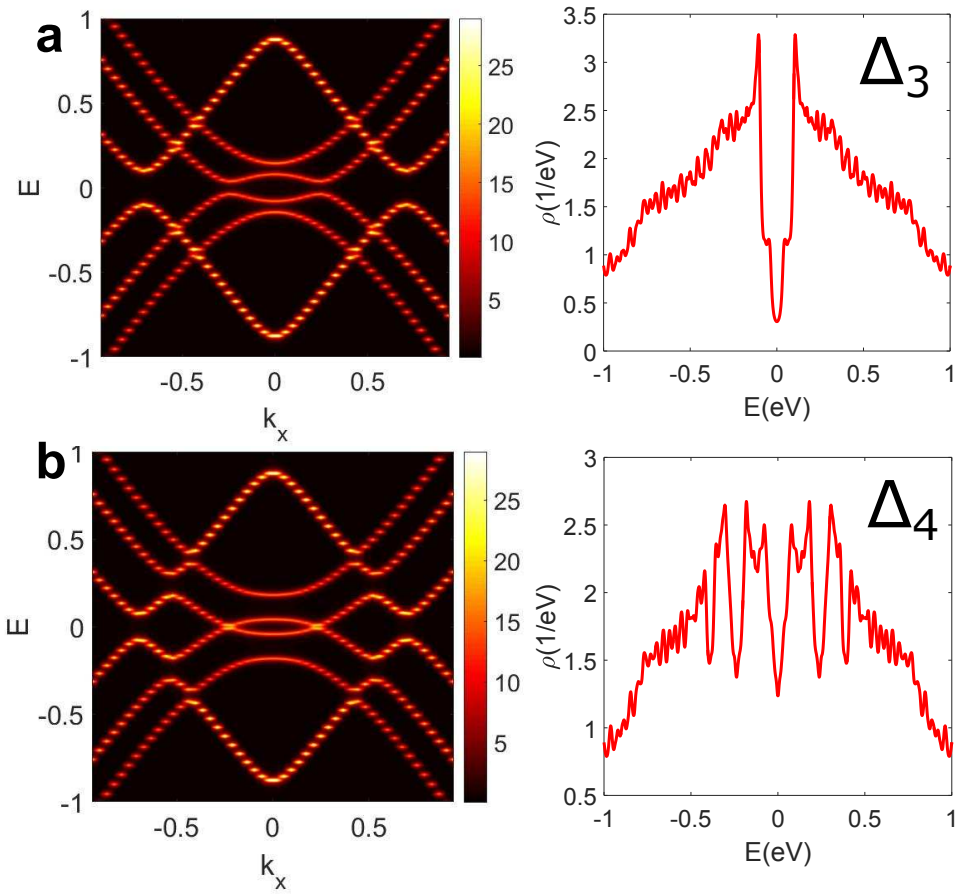

Figure S6: Spectral function(Left panel) and surface density of states(right panel) for a TI slab with superconducting pair potentials (a) Δ_3 and (b) Δ_4

F. Variation of ripple structure with superconducting gap amplitude

The positions of the dips and peaks of the ripples depend not only on the sub-band structure of BSTS and the local gap that opens up at the avoided crossing, but also the primary superconducting gap that opens up at zero energy. Intuitively, the opening of the primary superconducting gap at zero energy pushes out the bulk sub-band energy levels away from the gap. As the value of the superconducting gap amplitude is diminished, for example, with increasing temperature, the sub-band energy levels are drawn closer to zero energy. This shifts the entire peak-dip structure closer towards zero energy with increasing temperature. This is simultaneously accompanied by the decrease of the local gap amplitude at the avoided crossings brings the two peaks associated with the dip closer together. However, since the gap amplitude at the avoided crossing is much smaller than

the primary superconducting gap amplitude, the overall effect is the shift of the super-gap peak-dip structures towards zero energy with increasing temperature, as observed in our experiment.

To illustrate this point, we provide simulations with model parameters as before chosen for theoretical convenience and clarity of understanding. We use the following model parameters: $A_1 = 1, A_2 = 1.5, B_1 = -0.5, B_2 = -0.75, D_1 = D_2 = 0, M = -0.8, \mu = 14$, TI slab of thickness $N = 5$ layers, pairing potential of type Δ_4 and vary the superconducting gap amplitude Δ from 0.05eV to 0.2eV and study the variation of the positions of the peak-dip structure of the super-gap ripples. The results are depicted in S7(a).

Our simulations reveal that the super-gap ripples not only decrease in depth with decreasing gap amplitude, but also shift progressively towards zero energy because of the collapse of the primary superconducting gap. Specifically, the peaks P1 and P2, and the associated dip, D1, (dotted box in S7(a)) all move towards zero energy. The shift in the positions of the P1, P2 and D1 is depicted in S7(b). As a function of the superconducting gap amplitude Δ, the positions of the peaks and dips decrease almost linearly as shown in S7(c). This behavior is in complete agreement with our experimental observation that the positions of the ripples observed in our experiment progressively move towards zero energy as the primary superconducting gap collapses.

G. Estimation of energy scale of super-gap ripples in a realistic BSTS/$NbSe_2$ junction

It is evident from the discussion in the previous section that the appearance of ripples at energy values larger than the superconducting energy gap do not admit a simple analytical formula that can be used to derive their exact positions. In fact, the positions of the conductance ripples are determined by the overlap of the topological surface state bands with the 2D bulk-like bands. Therefore, to aid meaningful comparison of our theory with experiments ,we now provide an energy scale estimation of the positions of the super-gap dI-dV ripples observed in our experiment. The flakes of BSTS studied in this work are $N_z \sim 50$ quintuple layers thick. While considering the band-structure of a BSTS/$NbSe_2$junction, we must take into account the work-function mismatch

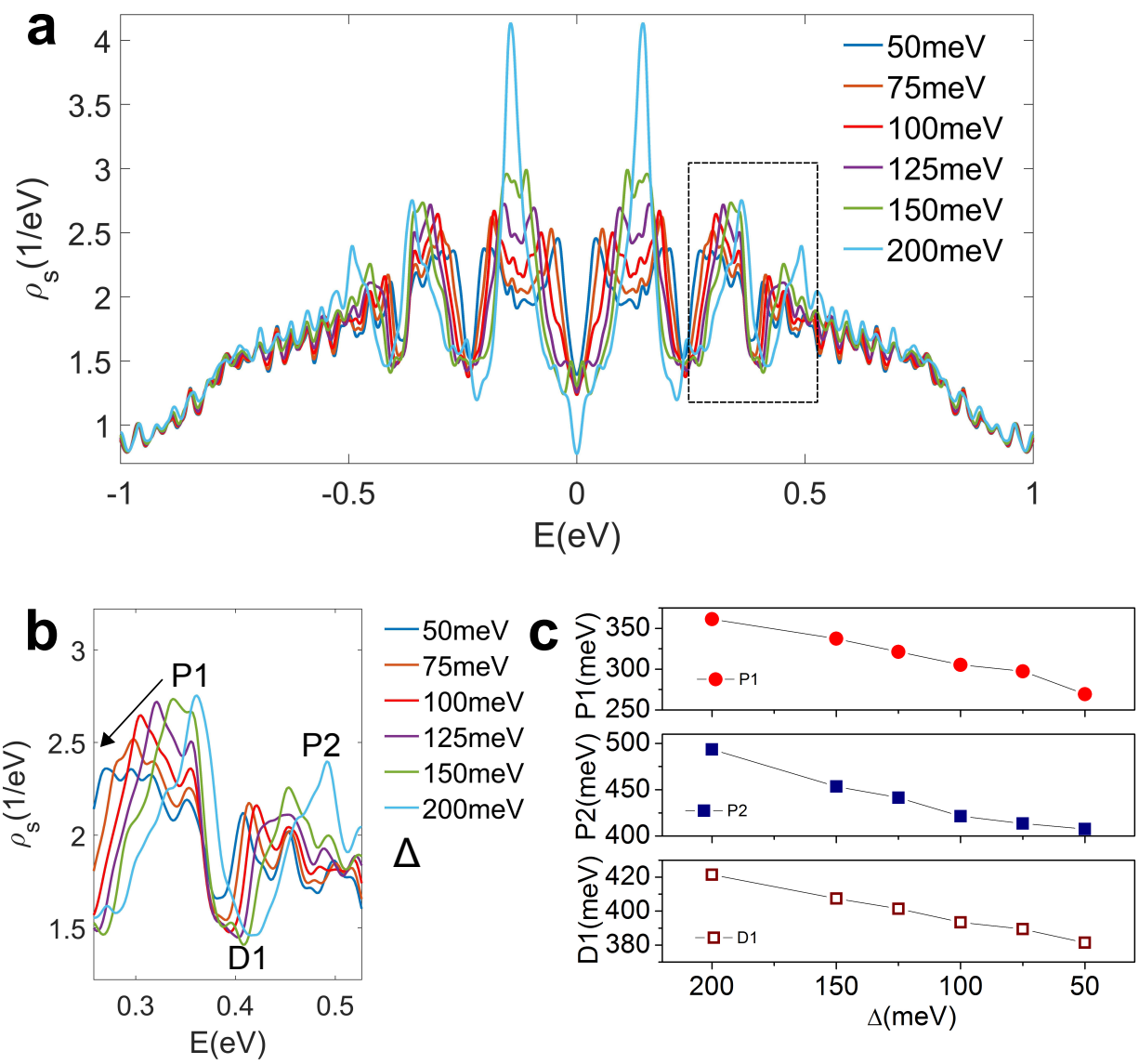

Figure S7: (a) Surface density of states for a TI slab (N=5 layers) with superconducing gap amplitude Δ varied from 200meV to 50meV (b) Shift of super-gap peaks P1 and P2 and associated dip D1 towards zero energy with decrease in superconducting gap amplitude (c) Positions of P1, P2 and D1 as a function of decreasing Δ

between the two materials, that decides the position of the chemical potential within the BSTS laer. The work-function of $NbSe_2$ is ϕ_{SC} =5.6-5.9 eV[13,14] whereas the work-function of BSTS is estimated to be ϕ_{TI} =5.0-5.1 eV.[15] This leads to p-type doping of the BSTS layer with a large bias $\simeq \phi_{SC} - \phi_{TI} = 0.5 - 0.9$eV. This potential difference is accommodated by pushing the chemical potential in BSTS close to the valence band maximum where the Fermi level gets pinned, and the

excess electrostatic potential is balanced by bulk-like carriers. We must therefore consider the sub-band structure near the valence band of BSTS, and estimate the separation between the sub-band energy levels for a 50 quintuple layer thick BSTS sample. This energy scale would then roughly correspond to the energy scale of the ripples in our experiment.

An accurate simulation of the BSTS band-structure is not possible, even through density functional theory because of the alloyed nature of the material. However, from band-structure calculations on the parent topological insulator Bi_2Se_3, it is known that the valence band is composed of J=1/2 Se atomic p-type orbitals, with each Bi_2Se_3 unit cell (corresponding to 1 QL) contributing one state (the two equivalent Se, +1/2 and Se, -1/2 orbitals contribute 2 states that are degenerate, effective leading to 1 energy state per QL). The bandwidth of the Se(1/2) valence bands is known to be $\Delta_{VB} \simeq 200$ meV with a strong concentration of sub-bands near the valence band maxima (VBM) from both theoretical calculations[16] and our own ARPES experiments on single crystals of $BiSbTe_{1.25}Se_{1.75}$ reported in Ref.[17] . Ignoring the concentration of sub-bands near the VBM, we obtain a lower limit on the energy spacing between neighboring sub-bands as $\Delta_{SB} \simeq \Delta_{VB}/N_z \simeq 4$meV where $N_z = 50$ is the number of quintuple layers of the TI slab. This estimation of the energy scale is in solid agreement with the experimentally measured energy separation of ripples of the order 2-5meV.

H. Bogoliubov-de Gennes spectrum of a realistic BSTS/$NbSe_2$ junction

To provide a quantitative estimation of the sub-band spectrum, we first tune our BHZ model parameters[6] for the normal state Hamiltonian h_0 to match our experimentally measured ARPES spectrum of BSTS,[17] especially near the valence band where our chemical potential lies as depicted in S8(a). We fit the parameters to match the experimentally measured bulk-valence band width ($\simeq$200meV), the position of the valence band maximum ($k_x \simeq 0.15$), the energy separation between the Dirac point and the Valence Band maxima ($\simeq$50 meV), and the velocity at the Dirac point (0.25 eV-). We obtain the following parameters for our model: $A_1 = 35$meV; $A_2 = 50$meV, $B_1 = -100$meV; $B_2 = -50$ meV; and $M_0 = -50$ meV. The theoretically calculated band-structure

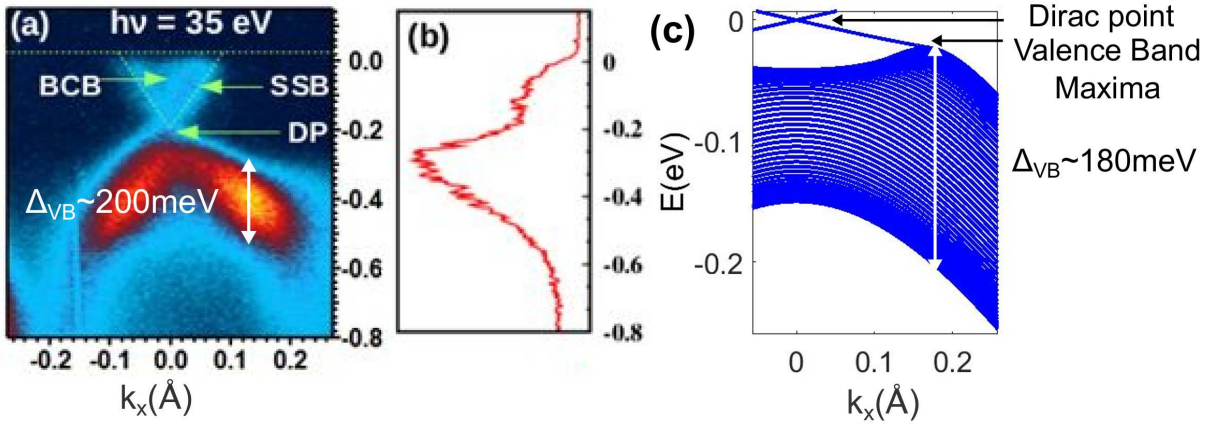

Figure S8: (a) ARPES image taken at photon energy 35eV near the chemical potential indicated by zero energy (b) Energy dispersion curve corresponding to the ARPES data presented in (a). (c) Tight-binding simulation of the BHZ model to simulate the experimentally observed band-structure near the valence band. Figures (a) and (b) are obtained from Lohani *et al.*[17] published under the Creative Commons Attribution 4.0 International License found here

is depicted in S8(c). Note that in the calculations we set the Dirac point to zero energy whereas for the experimentally measured spectrum, the chemical potential is defined to be zero energy.

Using these band-structure parameters we perform Green's function based calculation of the Bogolubov-de Gennes spectrum of a realistic BSTS/$NbSe_2$ junction. The value of the chemical potential is set to the position of the valence band maxima $\mu = 40$ meV below the Dirac point, and the superconducting gap is set as a Δ_2-type pairing potential with $\Delta = 2.0$meV. The results for the obtained surface spectral function and surface density of states for a TI slab with $N_z = 50$ quintuple layers is presented in Fig. 5 of the main text. Here we provide additional simulations performed on TI slabs with thicknesses $N_z = 20$ and $N_z = 35$ quintuple layers as depicted in S9(a) and S9(b) respectively.

In all our simulations, we observe clear signatures of density of states oscillations that appear because of avoided crossings between the topological surface state and the 2D bulk sub-bands. For $N_z = 20$, the energy spacing between ripples is $\simeq$4-5meV wheras for $N_z = 35$ the energy spacing is $\simeq$ 2-3meV. This is in complete agreement with the arguments presented in Sec.H where we had estimated that the energy spacings of the dI-dV ripples scale as $\propto \frac{1}{N_z}$.

I. Raw differential conductance data

In the main text, we have provided the differential conductance data as a function of the DC bias voltage where the voltage drop across the un-proximitized part of the topological insulator lead is taken into account by estimating the lead resistance R_l. Error in the estimation of R_l can lead to a shift of the voltage bias positions of various features obtained in the dI-dV data and also lead to a change in their amplitude. To account for this ambiguity, we provide the raw differential conductance data as a function of the DC bias corrected and the uncorrected DC bias voltage.

In S10, S11 and S12 we provide the raw differential conductance data measured as a function of the DC bias current.

In S13 and S14 we provide the raw differential conductance data as a function of the DC bias voltage obtained by integrating the DC current biased differential conductance data.

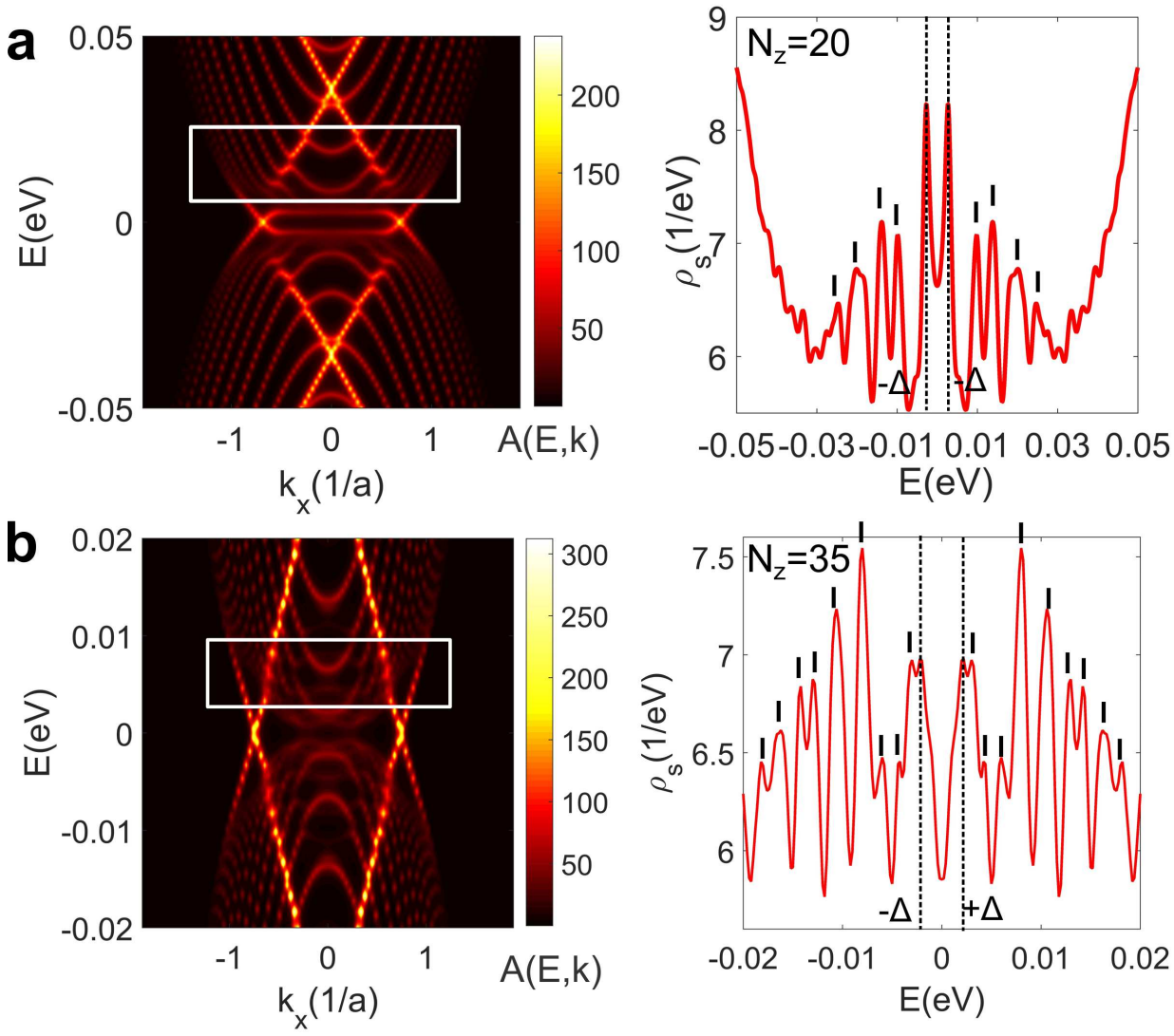

Figure S9: (Left-panel) Surface spectral function evaluated for a realistic interface between $NbSe_2$ and BSTS and (Right-panel) corresponding density of states showing oscillations arising as a consequence of topological superconductivity for (a) 20 QL and (b) 35 QL thick slab of BSTS. The 2D Majorana type surface Andreev bound state are clearly visible at zero energy. The white boxes in the left panels depict the avoided crossings between the topological surface state and bulk derived 2D sub-bands

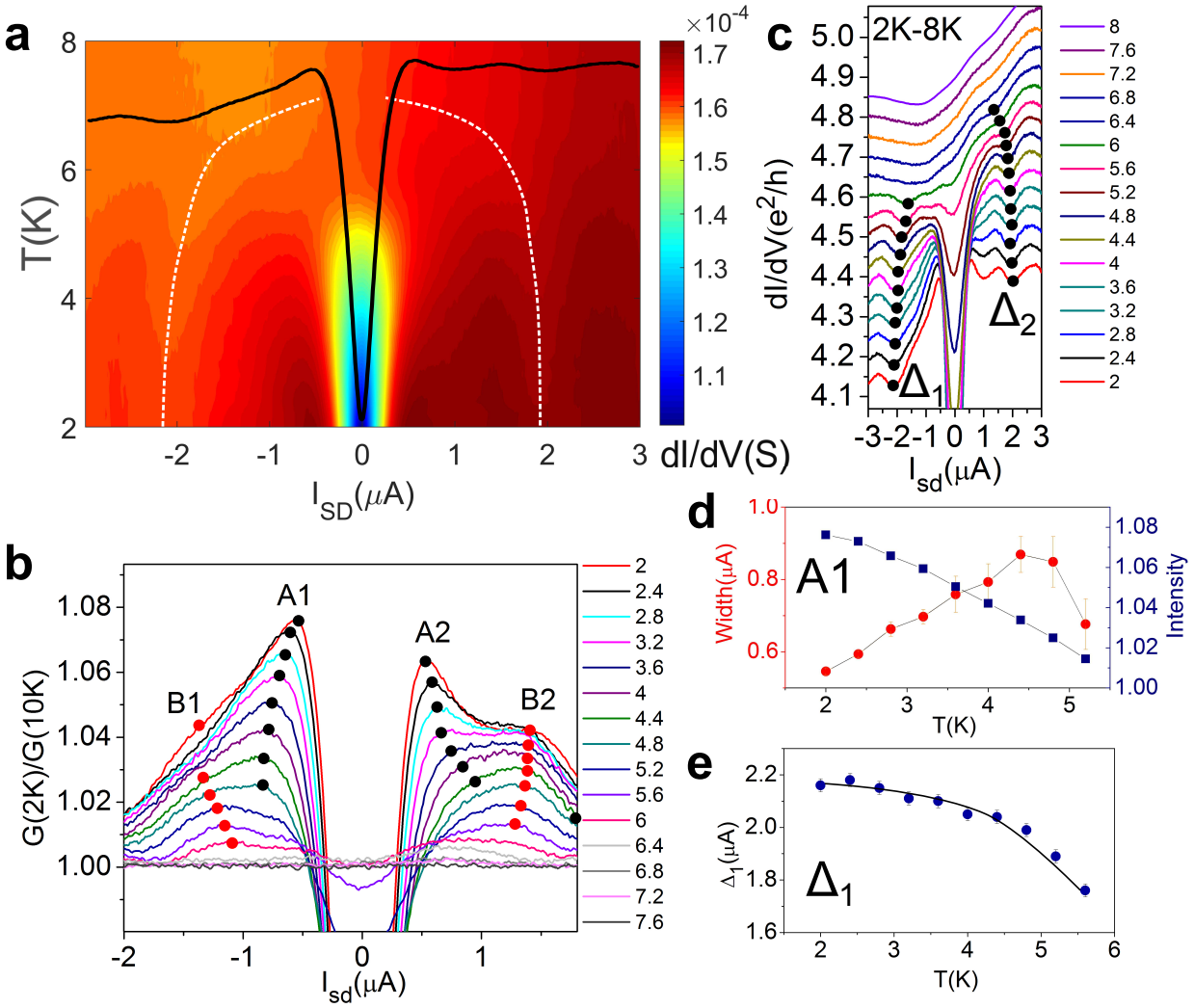

Figure S10: (a) 2D color plot of differential conductance as a function of temperature and source-drain DC current bias I_{SD} (b) Normalized differential conductance G(2K)/G(10K) showing a two-gap structure. The black and red dots track the evolution of coherence-like peak A1(A2) and B1(B2) respectively (c) Differential conductance ripples Δ_1 and Δ_2 that exist at biases larger than the superconducting gap. Black dots trace their evolution with increasing temperature. (d) Evolution of the width and intensity of peak A1 with increasing temperature (e) Evolution of position of the conductance dip at Δ_1 with increasing temperature.

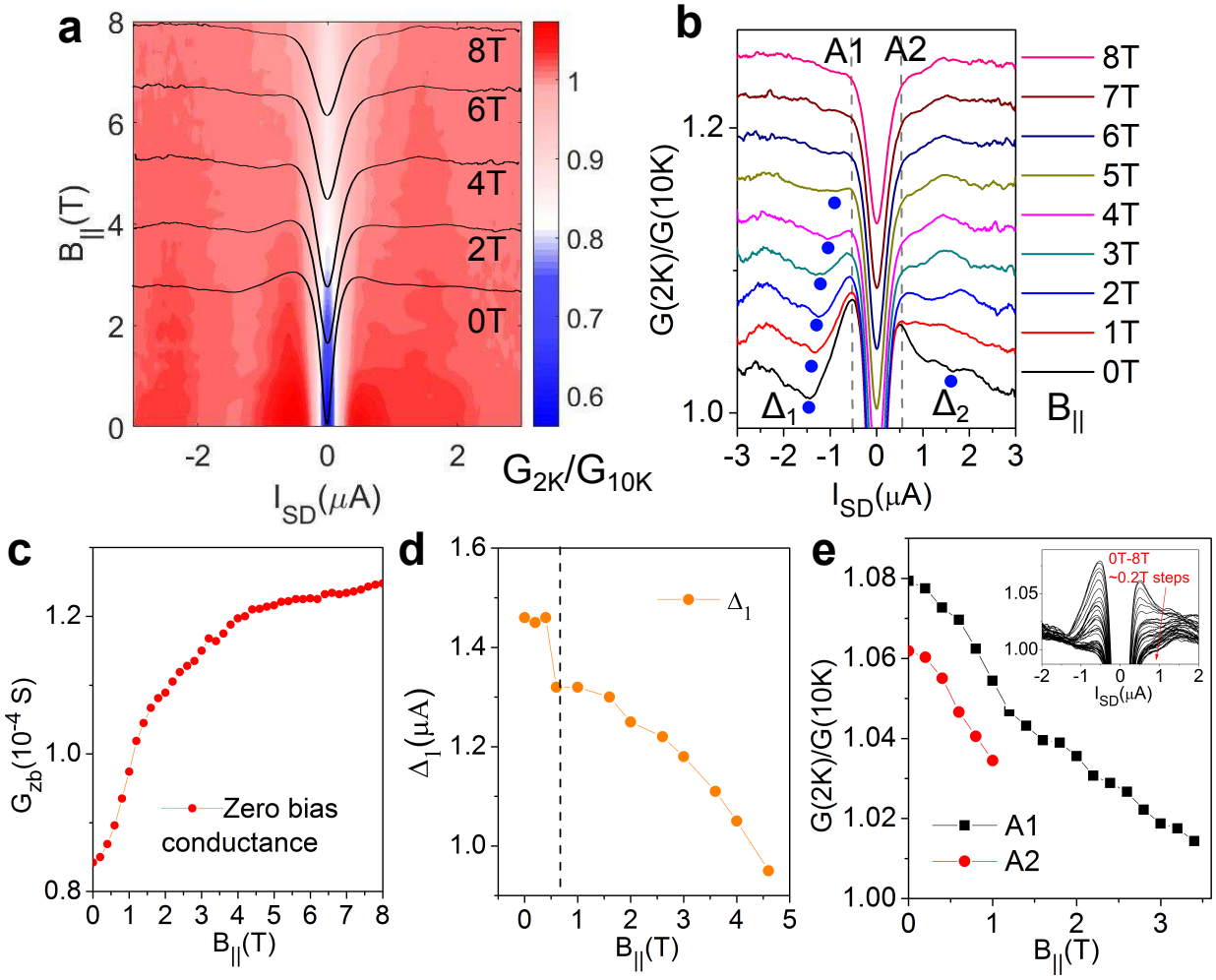

Figure S11: (a) 2D color plot of normalized differential conductance G(2K)/G(10K) vs I_{SD} as a function of in-plane magnetic field. (b) Evolution of G(2K)/G(10K) showing the breakdown of asymmetry with increasing in-plane magnetic field. The super-gap ripples at Δ_1 and Δ_2 marked as blue dots also disappear. (c) Zero bias conductance G_{zb} as a function of in-plane magnetic field. (d) Evolution of bias position of dip at Δ_1 with $B_{||}$. (e) Evolution of normalized coherence peak intensity at A1 and A2 with $B_{||}$.

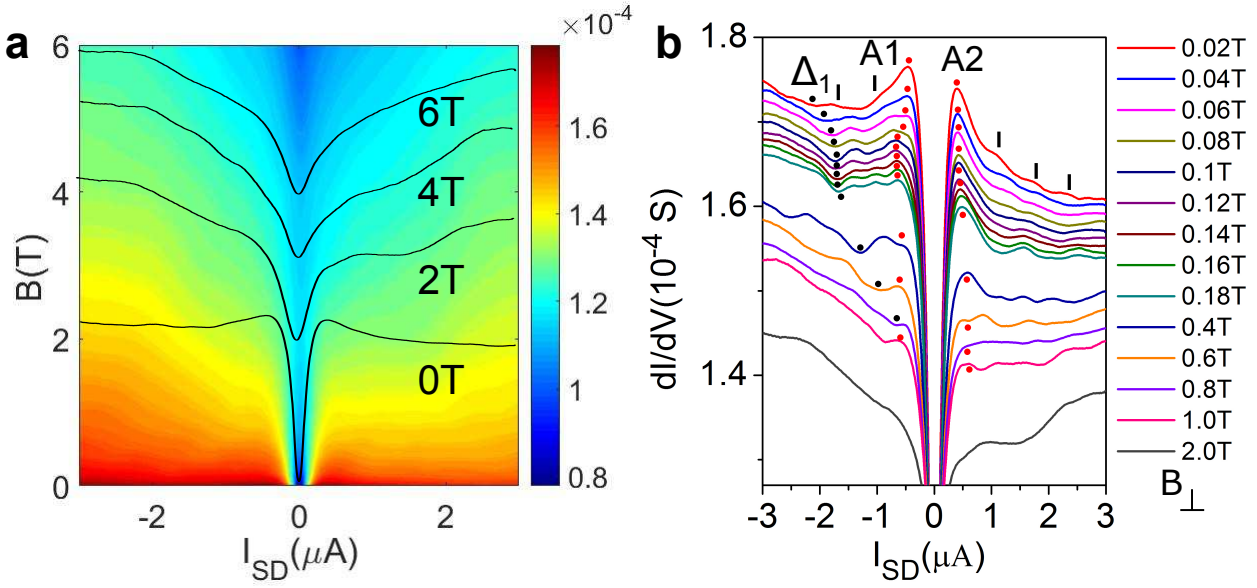

Figure S12: (a) 2D color plot of differential conductance as a function of out-of-plane magnetic field from 0T to 8T and DC current bias I_{SD} (b) Low field(0T-2T) evolution of differential conductance spectrum showing several ripples at super-gap biases marked by vertical solid lines

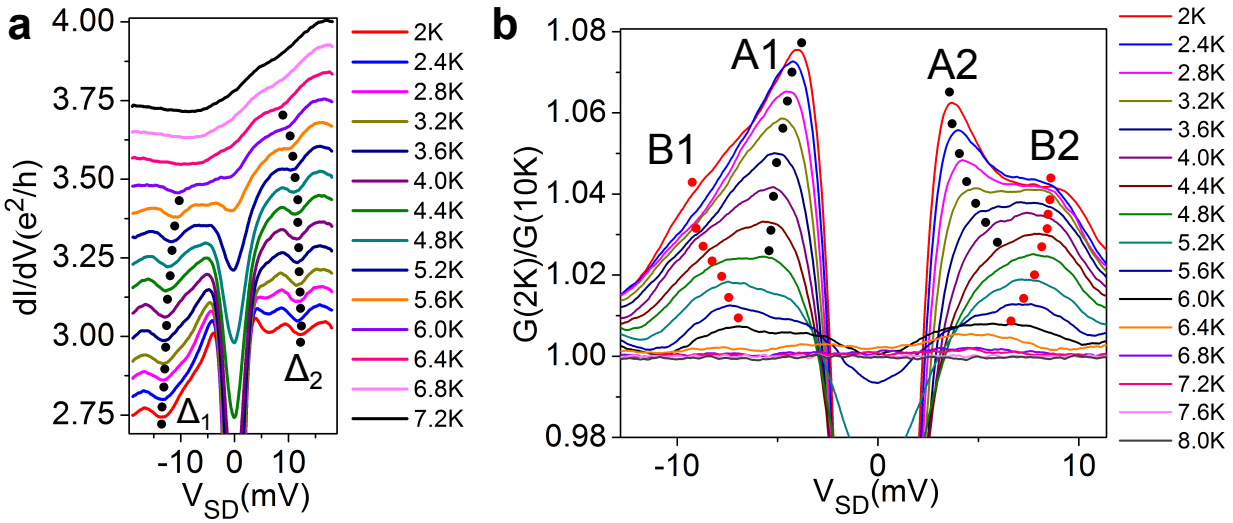

Figure S13: (a) Raw differential conductance data as a function of uncorrected source-drain bias voltage V_{SD}, showing ripples Δ_1 and Δ_2 that exist at biases larger than the superconducting gap. Black dots trace their evolution with increasing temperature.(b) Normalized differential conductance G(2K)/G(10K) showing a two-gap structure. The black and red dots track the evolution of coherence-like peak A1(A2) and B1(B2) respectively

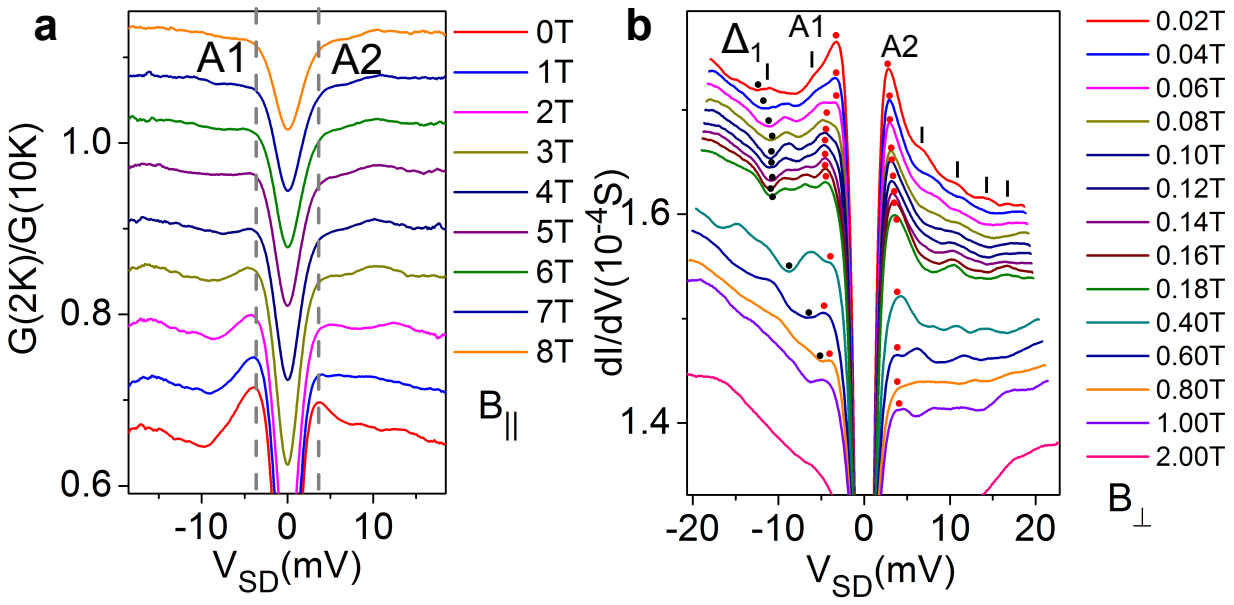

Figure S14: (a) Evolution of normalized differential conductance G(2K)/G(10K) as a function of uncorrected source-drain voltage bias V_{SD} showing the breakdown of differential conductance asymmetry with increasing in-plane magnetic field. (b) Evolution of differential conductance spectrum as a function of perpendicular magnetic field showing several ripples at super-gap biases marked by vertical solid lines

References

[1] Blonder, G.; Tinkham, M.; Klapwijk, T. Transition from Metallic to Tunneling Regimes in Superconducting Microconstrictions: Excess Current, Charge Imbalance, and Supercurrent Conversion. *Phys. Rev. B* **1982**, *25*, 4515–4532.

[2] Stehno, M. P.; Hendrickx, N. W.; Snelder, M.; Scholten, T.; Huang, Y.; Golden, M. S.; Brinkman, A. Conduction Spectroscopy of a Proximity Induced Superconducting Topological Insulator. *Semicond. Sci. Technol.* **2017**, *32*, 094001.

[3] Tikhonov, E.; Shovkun, D.; Snelder, M.; Stehno, M.; Huang, Y.; Golden, M.; Golubov, A. A.; Brinkman, A.; Khrapai, V. Andreev Reflection in an s-Type Superconductor Proximized 3D Topological Insulator. *Phys. Rev. Lett.* **2016**, *117*, 147001.

[4] Krogstrup, P.; Ziino, N.; Chang, W.; Albrecht, S.; Madsen, M.; Johnson, E.; Nygård, J.; Marcus, C.; Jespersen, T. Epitaxy of Semiconductor-Superconductor Nanowires. *Nat. Mater.* **2015**, *14*, 400–406.

[5] Shabani, J.; Kjaergaard, M.; Suominen, H. J.; Kim, Y.; Nichele, F.; Pakrouski, K.; Stankevic, T.; Lutchyn, R. M.; Krogstrup, P.; Feidenhans'l, R.; Kraemer, S.; Nayak, C.; Troyer, M.; Marcus, C.M.; Palmstrom, C.J. Two-Dimensional Epitaxial Superconductor-Semiconductor Heterostructures: A Platform for Topological Superconducting Networks. *Phys. Rev. B* **2016**, *93*, 155402.

[6] Zhang, H.; Liu, C.-X.; Qi, X.-L.; Dai, X.; Fang, Z.; Zhang, S.-C. Topological Insulators in Bi_2 Se_3, Bi_2Te_3 and Sb_2Te_3 with a Single Dirac Cone on the Surface. *Nat. Phys.* **2009**, *5*, 438–442.

[7] Fu, L.; Berg, E. Odd-Parity Topological Superconductors: Theory and Application to $Cu_xBi_2Se_3$. *Phys. Rev. Lett.* **2010**, *105*, 097001.

[8] Hao, L.; Lee, T. Surface Spectral Function in the Superconducting State of a Topological Insulator. *Phys. Rev. B* **2011**, *83*, 134516.

[9] Nakosai, S.; Tanaka, Y.; Nagaosa, N. Topological Superconductivity in Bilayer Rashba System. *Phys. Rev. Lett.* **2012**, *108*, 147003.

[10] Hsieh, T. H.; Fu, L. Majorana Fermions and Exotic Surface Andreev Bound States in Topological Superconductors: Application to $Cu_xBi_2Se_3$. *Phys. Rev. Lett.* **2012**, *108*, 107005.

[11] Yada, K.; Sato, M.; Tanaka, Y.; Yokoyama, T. Surface Density of States and Topological Edge States in Noncentrosymmetric Superconductors. *Phys. Rev. B* **2011**, *83*, 064505.

[12] Sasaki, S.; Kriener, M.; Segawa, K.; Yada, K.; Tanaka, Y.; Sato, M.; Ando, Y. Topological Superconductivity in $Cu_xBi_2Se_3$. *Phys. Rev. Lett.* **2011**, *107*, 217001.

[13] Liu, Y.; Stradins, P.; Wei, S.-H. Van der Waals Metal-Semiconductor Junction: Weak Fermi Level Pinning Enables Effective Tuning of Schottky Barrier. *Sci. Adv.* **2016**, *2*, e1600069.

[14] Shimada, T.; Ohuchi, F. S.; Parkinson, B. A. Work function and Photothreshold of Layered Metal Dichalcogenides. *Jpn. J. Appl. Phys.* **1994**, *33*, 2696–2698.

[15] Takane, D.; Souma, S.; Sato, T.; Takahashi, T.; Segawa, K.; Ando, Y. Work Function of Bulk-Insulating Topological Insulator $Bi_{2-x}Sb_xTe_{3-y}Se_y$. *Appl. Phys. Lett.* **2016**, *109*, 091601.

[16] Acosta, C. M.; Lima, M. P.; da Silva, A. J. R.; Fazzio, A.; Lewenkopf, C. H. Tight-binding Model for the Band Dispersion in Rhombohedral Topological Insulators over the Whole Brillouin Zone. *Phys. Rev. B* **2018**, *98*, 035106.

[17] Lohani, H.; Mishra, P.; Banerjee, A.; Majhi, K.; Ganesan, R.; Manju, U.; Topwal, D.; Kumar, P. A.; Sekhar, B. Band Structure of Topological Insulator $BiSbTe_{1.25}Se_{1.75}$. *Sci. Rep.* **2017**, *7*, 4567.